Journal of Analytical and Applied Pyrolysis 133 (2018) 225–233

Contents lists available at ScienceDirect

Journal of Analytical and Applied Pyrolysis

journal homepage: www.elsevier.com/locate/jaap

Thermal decomposition of yttrium propionate: film and powder

Silvia Rasi[a,b,*], Susagna Ricart[b], Xavier Obradors[b], Teresa Puig[b], Pere Roura[a], Jordi Farjas[a]

[a] University of Girona, Campus Montilivi, Edif. PII, E17003 Girona, Catalonia, Spain
[b] Institut de Ciència de Materials de Barcelona, ICMAB – CSIC, Campus UA Barcelona, E-08193 Bellaterra, Catalonia, Spain

ARTICLE INFO

Keywords:
Yttrium propionate
Thermal analysis
TG-MS
TG-FTIR
Film pyrolysis
Thermal decomposition kinetics
Combustion

ABSTRACT

The processes involved in the thermal decomposition of yttrium propionate in oxidizing and inert atmosphere were analyzed with thermoanalytical techniques (thermogravimetry and evolved gas analysis) and with the help of structural characterization (X-ray diffraction, infrared spectroscopy and elemental analysis) of intermediate and final products. Samples in the form of films and powders were analyzed. The decomposition behavior studied as a function of particle size and film thickness was investigated. We conclude that, as a consequence of the gas and heat transport, films decompose differently than powders. Finally, two decomposition mechanisms are proposed that are in agreement with the observed volatiles and intermediate phases.

1. Introduction

The relatively recent interest in yttrium propionate (Y-Prop$_3$) has been boosted by its application in the synthesis of $YBa_2Cu_3O_{7-x}$ (YBCO) [1–3]. YBCO belongs to the second generation of high-temperature superconductors, which are applied in the form of tapes (also called coated conductors, CCs), and thus its entire synthetic process is based on thin film technology. Among the different processing routes, YBCO synthesis through chemical methods (chemical solution deposition, CSD) [4] provides the possibility, with respect to physical methods, for cost efficient and easily scalable processes.

CSD routes can be differentiated based on the type of YBCO precursor solution, which usually tends to involve short-chain carboxylates of the corresponding metals in order to facilitate the removal of the organic moieties during the first stage of the films' thermal treatment (pyrolysis). Since during the second stage (growth) the film is treated at much higher temperatures, the choice of the precursor solution plays a fundamental role in the type of intermediate species that are formed and therefore the subsequent choice of the experimental conditions (P,T) to facilitate their conversion to YBCO. In this regard, up to now, there is a wide understanding of the trifluoroacetate (TFA) route [5–7] to YBCO, where the precursor solution consists of the trifluoroacetate salts of each metal. However, a major drawback of this route is that the decomposition of the intermediate BaF_2 involves the release of Hydrofluoric acid (HF). It has been stated that out-diffusion of HF is the limiting step in obtaining YBCO during the growth stage [6–9]. The thicker the film, the more difficult HF removal is, so it is not possible to obtain a fast growth rate in thick films through the TFA route. Indeed, the slow HF diffusion is the main challenge in obtaining cost-competitive YBCO tapes. Therefore, other precursor solutions have been considered, such as low-fluorine [2] or fluorine-free (FF) solutions [10]. In fact, it has been shown that, from FF solutions, YBCO can grow through a liquid-solid reaction [11,12], and this in turn can lead to very high growth rates.

To get the final desired properties of the superconductive tapes, each stage of the synthetic process needs to be understood and optimized. In this perspective, thermal analysis (TA) is especially suited to monitor structural transformations such as solvent evaporation, precursor pyrolysis, oxidation and decomposition of intermediate compounds that take place during pyrolysis of metal-organic precursors. In fact, there have been an increasing number of studies regarding the thermal decomposition of YBCO FF-precursor powders such as Yttrium acetate (YAc$_3$), Yttrium propionate (YProp$_3$) and the corresponding barium and copper salts [13–15]. However, so far, the thermal decomposition of Y-Prop$_3$ has been studied only in the form of powder [16–19]. In situ evolved gas analysis (EGA) was performed by means of quadrupole mass spectrometry (EGA-MS/Q) by [17,18] in air and in nitrogen, and with Fourier-transform infrared spectroscopy (EGA-FTIR) in argon by [19]. The reported volatiles, even in inert atmosphere, are different, so that a univocal and general mechanism has not been established yet. Also the literature shows differences in the temperature range in which the last stage takes place, reporting complete decomposition at 600 °C [16–18], 700 °C [17] or even at 1350 °C [19]. Besides, despite the fact that water vapor is commonly used in the synthesis of YBCO FF tapes, none of the published papers analyze the effect of the presence of water vapor in the thermal decomposition of

* Corresponding author.
E-mail addresses: silvia.rasi@udg.edu, srasi@icmab.es (S. Rasi).

https://doi.org/10.1016/j.jaap.2018.03.021
Received 9 January 2018; Received in revised form 5 March 2018; Accepted 24 March 2018
Available online 27 March 2018

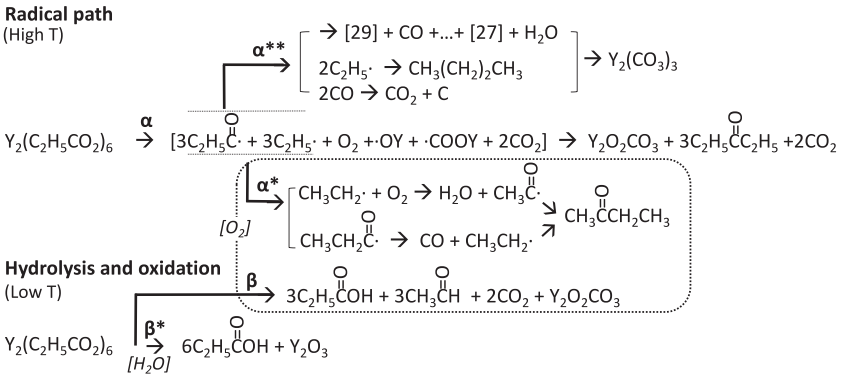

Fig. 1. Proposed reaction scheme for Y-Prop$_3$ decomposition.

the metalorganic precursor [3,20].

Moreover, the use of TA in films is quite limited because the signal-to-noise ratio depends on the sample mass, and sample mass for films is typically one order of magnitude smaller than sample mass used in TA experiments. However, it has been stated that powders can behave differently than films [9,21–25] due to different gas and heat transport phenomena between the two. Therefore, an in-situ study of the thermal processes that lead to YBCO tape synthesis is of fundamental interest to reveal the actual kinetics and mechanism occurring in films.

In this study, both in-situ EGA-MS/Q and EGA-FTIR are applied to analyze the volatiles formed during pyrolysis and the effect of different atmospheres. It will be shown that, depending on the surrounding atmosphere, two different mechanisms compete and involve the formation of different volatiles. In particular, the kinetics is significantly enhanced in the presence of water vapor. Additionally, gas transport also affects the kinetics and the relative contribution of a given reaction mechanism. A new reaction scheme will be proposed around the already known radical path of decomposition (Fig. 1, reaction **α**).

2. Material and methods

Yttrium acetate hydrate ($Y(CH_3CO_2)_3{\cdot}xH_2O$ Sigma Aldrich, 99.9%) was dried in vacuum at 55 °C and then dissolved ($[Y^{3+}] = 0.25$ M) in a mixture of methanol (VWR, 99.8%) and propionic acid (Merck, ≥99%), with a solvent proportion of 1:1 in volume. The solution was deposited by drop coating over 10 × 10 mm^2 $LaAlO_3$ (LAO) substrates and dried at 80 °C on hot plate for 5 min. Residual water and propionic acid may not be completely removed at this stage, depending on the thickness of the film. Due to the excess of propionic acid, acetate groups are replaced by propionates [2]. Nominal thickness of films (h) reported in this work is calculated from the mass of the films, knowing the particle density of Y_2O_3 (d = 5.01 g/cm^3) and the surface area (A) of the substrate, h = m/(d·A). The nominal thickness is expected to be smaller than the real thickness due to the porosity of the films. Additionally, Y$(C_2H_5CO_2)_3$ (Y-Prop$_3$) powder precipitating over time from the same solution and left in atmospheric air to dry was studied as a comparison after grinding, unless else indicated. Particles' size for ground powders is ≈10 μm, for not-ground is between 0.1 and 1 mm.

Thermogravimetric experiments (TG) were carried out in a Mettler Toledo thermobalance, model TGA/DSC1. FTIR evolved gas analysis (EGA-FTIR) was performed with a Bruker model ALPHA spectrometer coupled to a gas cell (Transmission model). A steel tube kept at 200 °C was used to connect the thermobalance to the gas cell. Sample temperature was raised at a constant rate (shown in the corresponding EGA figures) up to 600 °C under a continuous flow (55 ml/min) of the desired gas. Uncovered Al_2O_3 pans of 70 μl in volume were used for samples in the form of powder, whereas LAO substrates 10 × 10 mm^2 were used for film deposition. EGA-FTIR results are reported plotting the wavenumber corresponding to the most characteristic, but not necessarily the most intense, peak of each volatile as a function of temperature. FTIR frequencies referenced throughout the paper are the following: 1780 cm^{-1} for propionic acid, 2355 cm^{-1} for CO_2, 2740 cm^{-1} for acetaldehyde, 1732 cm^{-1} for 3-pentanone and 2-butanone, 2180 cm^{-1} for CO.

In the case of TG analysis coupled with mass spectrometry (EGA-MS), alumina pans of 150 μl were used as crucibles and a steel capillary heated up to 200 °C was used to connect the TG gas outlet to the MS chamber. In the case of EGA-MS of films decomposed in vacuum (total pressure around 10^{-7} bar), the sample deposited on 5 × 5 mm^2 LAO was heated up in a quartz tube directly connected to the MS chamber. The vacuum was achieved with a turbomolecular pump in series with a rotary pump. In both cases, EGA-MS experiments were performed by means of a quadrupole analyzer (MKS model Microvision Plus).

Five experiments were conducted on films: for EGA-FTIR experiments, the sample was decomposed at 5 K/min at atmospheric pressure of humid oxygen (**A**), dry oxygen (**B**) and dry nitrogen (**C**); for EGA-MS experiments, the films were heated up at 5 K/min in an atmosphere of oxygen with a total pressure of 10^{-5} bar (**E**) and in an atmosphere of air with total pressure of 10^{-7} bar (**F**). Powder samples (labeled with a single quote (')) were decomposed in crucibles at atmospheric pressure of inert gas (**D'**, nitrogen for EGA-FTIR at both 5 and 10 K/min and argon for EGA-MS at 10 K/min) and oxygen (**C'**, EGA-FTIR-MS, 10 K/min). In the case of D', since EGA-FTIR gave similar results using Ar or N_2, Ar was chosen for the corresponding EGA-MS experiment to avoid interference with CO (m/z = 28, as N_2).

Differential Scanning calorimetry (DSC) was performed for powders with a Mettler Toledo model DSC822, in 70 μl-alumina pans, in the same experimental conditions as the corresponding TG experiment. For films, the DSC signal came directly from the TGA/DSC experiment.

Infrared spectra of solid samples were collected using a Fourier Transform Infrared Spectrometer (FTIR), Bruker model ALPHA coupled to an attenuated total reflection (ATR) module (model Platinum ATR). XRD experiments were done in a D8 ADVANCE diffractometer from Bruker AXS. The X-ray beam wavelength was 1.5406 Å (Cu-Kα). The X-ray source was operated at a voltage of 40 kV and at a current of 40 mA. Elemental Analysis was performed in a Perkin Elmer 2400 series elemental analyzer.

3. Results and discussion

3.1. Characterization of initial product

The FTIR and XRD pattern of as-deposited Y-Prop$_3$ are shown in Fig. 2a and b, respectively. Since the FTIR spectra of both the film and powder samples are nearly identical, their chemical structures are expected to be the same; both show the appearance of the propionate stretching bands (absent in the acetate). Also the results from elemental analysis (Table 1) of the dry Y-Prop$_3$, obtained from the corresponding Y-Ac$_3$ solution, agree with the expected composition of Y-Prop$_3$, providing further support for the replacement of acetate groups by

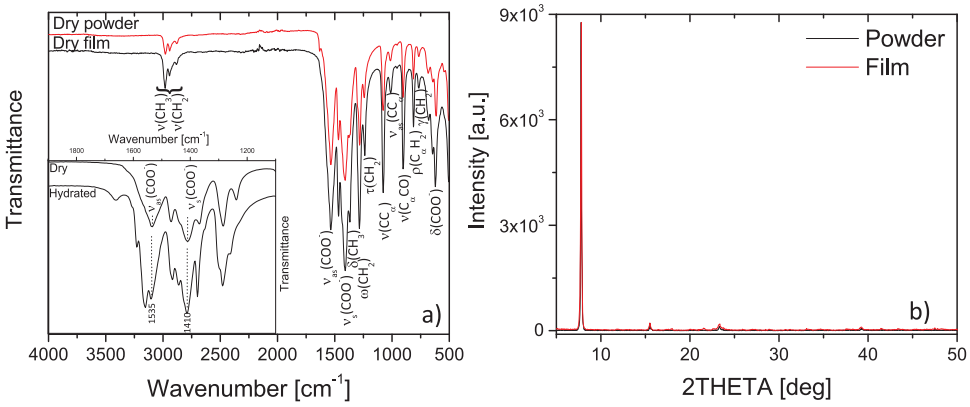

Fig. 2. a) Infrared spectra and b) XRD of the film and powder initial product.

Table 1
Elemental analysis of initial compounds and products obtained from decomposition in oxygen (**B**), nitrogen (**D'**) at 600 °C and vacuum (**F**) at 500 °C. The expected values for anhydrous Y-Ac_3 and Y-$Prop_3$ are included. Compositions are given in mass percent.

Compound	Found (Expected)	
	%C	%H
Y-Ac_3 (anhydrous)	(27.09)	(3.41)
Y-$Prop_3$ (anhydrous)	34.36 (35.08)	4.59 (4.91)
B (600 °C)	0.98	–
D' (600 °C)	0.33	–
F (500 °C)	9.69	–

propionates. Conversely, although the XRD pattern of the present work is similar to [19], there are significant differences between our FTIR and XRD pattern and those reported in the literature [16–19], also there are significant differences among the different structures reported in the literature. Indeed, in carboxylates, the carboxylate bond and the crystalline structure depend strongly on the presence of crystallization water [2,26–28], so that the distance between the asymmetric and symmetric carboxylic bands [$\Delta\nu = \nu_{as}(COO^-) - \nu_s(COO^-)$] can be used to determine the type of carboxylate-to-metal complexation structure [27,29–32]. Thus, for propionates, by comparison between $\Delta\nu$ and that of sodium propionate ($\Delta\nu_{Na\text{-}prop} = 134.6\,cm^{-1}$) [33] it has been proposed that [27,30] a chelating coordination exists when $\Delta\nu << \Delta\nu_{Na\text{-}}$prop, bridging coordination occurs when $\Delta\nu \leq \Delta\nu_{Na\text{-}prop}$, while monodentate coordination appears when $\Delta\nu >> \Delta\nu_{Na\text{-}prop}$.

Nasui et al. [29] obtained $\Delta\nu = 135\,cm^{-1}$, which was assigned to a mixed structure of chelating and bridging. From XRD, Martynova et al. [32] found three different coordination modes for the carboxylate ligands in Y-$Prop_3$ monohydrate: tridentate chelating-bridging, bidentate chelating and bidentate bridging, reporting a splitting of ν_{as}(COO-) and ν_s(COO-) in three bands that can be assigned to these different structural functions of the ligand. In this work, the shape of ν_{as}(COO-) and ν_s(COO-) of the dry salt does not show a clear splitting, but different coordination modes that are compatible with the results of Nasui and Martynova are nevertheless present. In fact, from the FTIR spectra of our dry Y-$Prop_3$ films (Fig. 2a), $\Delta\nu = 125\,cm^{-1}$, suggesting the presence of a bidentate chelating coordination mixed with some bridging coordination.

It is important to note that the modes of the carboxylate binding depend on the presence of crystallization water (see Fig. 2 inset and Fig.S1 in Supporting Info) but, since decomposition is not coupled to dehydration, once dehydration is completed, the evolution of the decomposition of the propionate should be independent of the initial structure and water amount.

3.2. Dehydration and solvent evaporation

The decomposition as a function of temperature, for films deposited on LAO substrates, was monitored by TG coupled to EGA-FTIR and EGA-MS.

For films, the first mass loss starts during the drying stage at 80 °C and corresponds to water and propionic acid evaporation; it is also observed by TG for thick films until 150 °C. This is expected since solvent removal depends on time and film thickness; in fact, the boiling point for the acid is relatively high (140 °C) and the remaining powder is very hygroscopic. Thus, between drying stage and TG experiment, atmospheric water may be absorbed (see the endothermic DSC peak in Fig. 3 at 65 °C that is related to water evaporation). The detailed description of dehydration can be found in the Supporting Info.

3.3. Thermal decomposition at atmospheric pressure: organic ligand

It has long been established that in inert atmosphere salts of carboxylic acids thermally decompose to yield CO_2 and symmetrical ketones as major products [34,35], following a free-radical reaction [36–38]. The same volatiles where observed by Grivel [19] for the thermal decomposition of Y-$Prop_3$ in Ar, proposing the reaction scheme **α** (radical) shown in Fig. 1: the mechanism results in a single dTG peak and an oxycarbonate intermediate that then yields yttria.

In agreement with this scenario, for Y-$Prop_3$ powder in inert atmosphere (both N_2 and Ar, Fig. 4D') we observe a single-step reaction around 355 °C where the main volatiles are 3-pentanone and CO_2 (by EGA-FTIR and EGA-MS), and it is in agreement with the presence of an endothermic peak in the DSC signal (Fig. 3) at 355 °C that is consistent

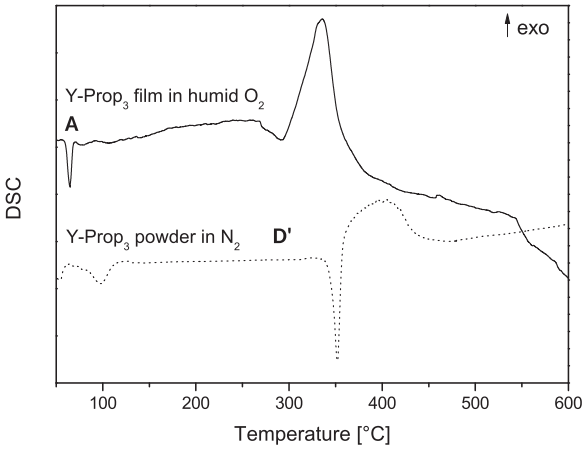

Fig. 3. Comparison of the DSC signal for Y-$Prop_3$ decomposition in experiments **A** and **D'**.

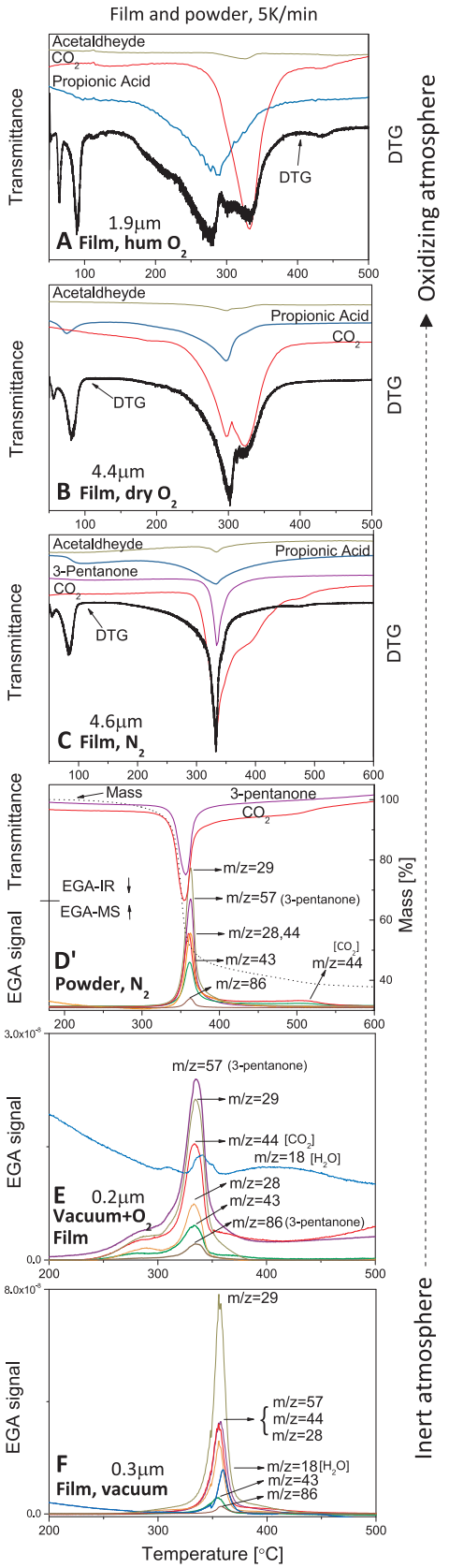

Fig. 4. EGA at 5 K/min for: Y-Prop$_3$ films in humid O_2 (**A**), dry O_2 (**B**), N_2 (**C**); powders in N_2/Ar (**D'**); films in $PO_2 \sim 10^{-5}$bar (**E**), $PO_2 < 10^{-7}$bar (**F**). Enlarged image of D' can be found in the Supporting Info.

with radicals formation. Thus, in inert conditions, the homolytic cleavage of the molecule and the recombination of the acyl and alkyl radicals would result in the formation of the symmetrical ketone 3-pentanone.

However, when the same compound is studied in inert conditions but after deposition on a substrate, the volatiles identified by IR are mainly propionic acid, along with the symmetrical ketone (Fig. 4C). Since both powder and film are obtained from the same solution, this difference can be attributed to the fact that films are much more sensitive to residual atmospheres than powders [21,39]. The effect of the residual oxygen was confirmed by increasing the flow of nitrogen in the TG; the higher the nitrogen flow, the higher the amount of 3-pentanone and the smaller the formation of propionic acid. Conversely, in a humid oxygen atmosphere, Fig. 4**A**, we observe that 1) the peak related to propionic acid is more prominent while 3-pentanone is no longer observed; 2) the evolution of propionic acid is shifted to lower temperatures and 3) the single step process in inert atmosphere becomes a two-step decomposition with splitting of the DTG signal into two peaks. IR analysis of volatiles shows that the first step is related mainly to the formation of propionic acid while the second step to CO_2 and acetaldehyde. The same behavior is observed with a flow of dry oxygen, although in this case the relative prominence of the first step is less significant than in the case of a humid atmosphere (Supporting Info, Fig.S6), and, for thicker films (~4 µm, Fig. 4**B**), the splitting is only evident in humid O_2, suggesting that water vapor favors the removal of the propionate groups as acid.

Since in the presence of oxygen degradative oxidation is likely to take place, for films in a dry O_2 atmosphere decomposition can be triggered by the oxidation of the propionate groups to acetaldehyde, CO_2 and propionic acid to produce the reaction scheme shown in **β** (Hydrolysis + oxidation) of Fig. 1. This is in agreement with the volatiles observed and the DSC signal in Fig. 3, which is no longer endothermic. Clearly, in humid O_2 and humid N_2 (not shown), the formation of propionic acid independent from acetaldehyde and CO_2 is due to the occurrence of mechanism **β*** in water vapor and low temperatures. However, **β*** does not reach completion in humid O_2 or in humid N_2 because, at higher temperatures, it is interrupted by the occurrence of **β** and **α**, respectively. Finally, in dry N_2 (**C**) and relatively thick films, 3-pentanone formation was observed with propionic acid and thus **β** and **α** (favored by the presence of residual O_2 and water vapor in the TG furnace) are competing, given the impossibility of creating a fully inert atmosphere in thin films [23,39].

3.4. Thermal decomposition at atmospheric pressure: oxycarbonate

Both paths, **α** and **β**, lead to the formation of an oxycarbonate (~ 44%): quenches of the solid residue in Fig. 5 at around 50% show the disappearance of CH_x groups with the increase of the COO^- stretching bands. From literature, yttrium carbonate decomposes to form yttrium oxycarbonates between 350 and 470 °C [40,41]. $Y_2O_2CO_3$ is stable up to 470 °C and decomposes in a single step to form yttrium oxide between 500 and 600 °C [42,43]. From Fig. 4**A** we observe a peak in the evolution of CO_2 around 440 °C for films in humid oxygen that can be attributed to the decomposition of $Y_2O_2CO_3$. Indeed, the observed mass loss and the FTIR spectra in Fig. 5 confirm this conclusion. Conversely, for films in nitrogen (Fig. 4**C**), we observe that the decomposition is completed at a higher temperature (470 °C) and two peaks related to the evolution of CO_2 are observed. This stage is much slower and gradual compared to experiments performed on films in O_2. The formation of CO_2 at higher temperatures is the result of the removal of carbon rich residues, which occurs through reaction with oxygen. Therefore, the more inert the atmosphere (and the longer the CO_2 out-diffusion path going from films to powder), the higher the final decomposition temperature. In fact, for the powder sample in nitrogen, the decomposition of the oxycarbonate is shifted to even higher temperatures (540 °C, Fig. 4**D'**), and the sample quenched at around 50%

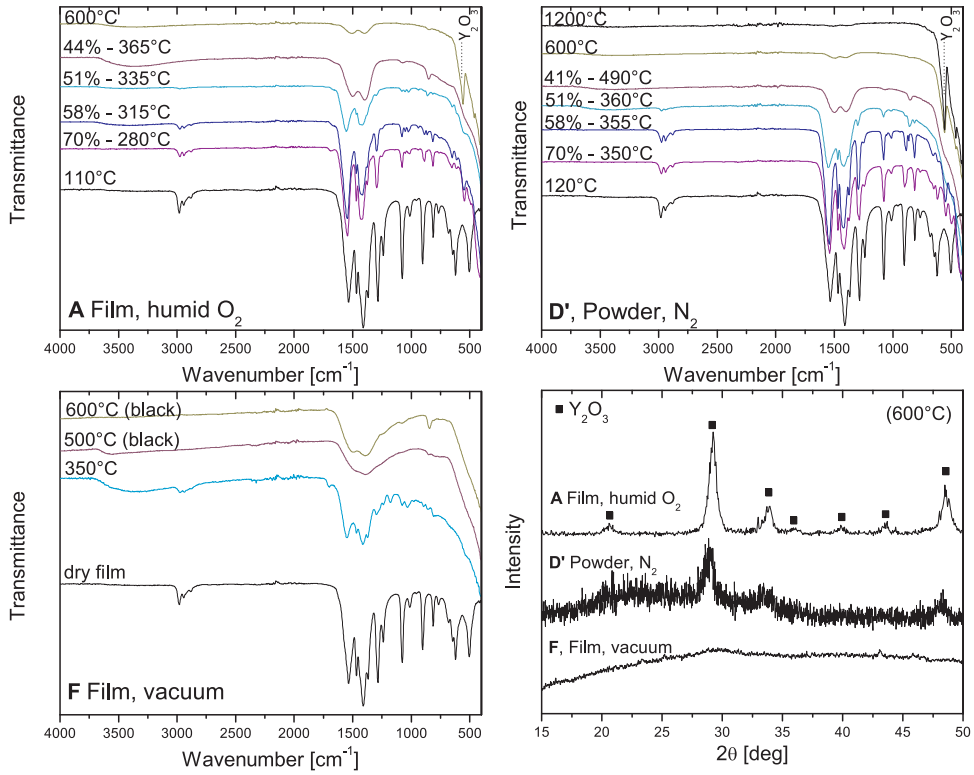

Fig. 5. FTIR of solid residue during Y-Prop$_3$ decomposition at 5 K/min in different atmospheres, and the corresponding XRD spectra of the final products. Percentages are expressed as (m_f/m_i)%.

(380 °C), is greyish, in agreement with the presence of some elemental carbon. On the other hand, quenches of the corresponding film in oxygen were white at both 50% and 41%.

These facts account for the different final decomposition temperatures reported in the literature. For instance, despite the fact that the XRD pattern shows the formation of Y_2O_3 at 600 °C (Fig. 5), the FTIR of the solid residue shows that decomposition is not fully completed at 600 °C for both powder and film; complete removal of COO- bands in the range 1400–1500 cm^{-1} is only observed after heating up to 1200 °C. Additionally, given the fact that, for films, more than one CO_2 peak is detected by EGA-FTIR, it is possible that, prior to the oxycarbonate, the decomposition passes through $Y_2(CO_3)_3$ and $Y_2O(CO_3)_2$ (Supp. Info, Fig.S7). A table summarizing the main temperature ranges of decomposition and mass loss can be found in the Supporting Info.

3.5. Vacuum and inert decomposition

Unlike the TG results previously discussed, when the decomposition is carried out in vacuum (Fig. 4**E** and **F**), the final product is no longer white but black. Although a black Y_2O_3 has been reported to form at low PO_2 due to oxygen substoichiometry [44], we can notice that elemental analysis (Table 1) shows that a significant amount of carbon is still present at 500 °C. This carbon could be attributed to elemental carbon (from disproportionation of CO) or a carbonate (expected ~10%C). Additionally, Fig. 5**F** shows that at 600 °C the Y-O FTIR band at 560 cm^{-1} is missing, while the contribution of broad bands in the conjugated carbonyl region is much more significant for experiments performed in vacuum (Fig. 5**F**) than in experiments performed at atmospheric pressure in oxidative, Fig. 5**A**, or inert atmosphere, Fig. 5**D'**.

The decomposition of the propionate in vacuum (Fig. 4**E** and **F**) produces again 3-pentanone (m/z = 57, 29, 86) and CO_2 (m/z = 44), along with C_2H_x fragments of m/z = 29 [C_2H_5], 28 (CO or [C_2H_4]), 27 [C_2H_3], 26 [C_2H_2] (not shown). Compared with **E**, in the highest vacuum (**F**) we notice a higher abundance of m/z = 29,28,27 with respect to 3-pentanone. Formation of CO instead of CO_2 would account for the greater COO- content in the product, while C_2H_5 formation in turn would explain the excess of m/z = 29 and the presence of m/z = 43, upon recombination to give butane (m/z = 43,29,28,27). Finally, in vacuum, radicals tend to survive longer due to a larger free path between collisions, and they may undergo further fragmentation (instead of recombining to form 3-pentanone or butane), explaining the excess of fragments m/z = 29 to 26, and water. All these competing reactions are displayed in **α**** (Fig. 1).

In fact, when some oxygen is introduced (Fig. 4**E**), the amount of fragments m/z = 26 to 29 decreases along with water. Reaction scheme α is favored with respect to carbonization, although not enough to remove all carbon and the final compound is still black, but its FTIR shows a small contribution from the characteristic Y_2O_3 band at 560 cm^{-1} (Supporting Info, Fig.S8).

Finally, at atmospheric pressure of Argon (Fig. 4**D'**) we observe some carbonization. In fact, although the final product is Y_2O_3 (white), the quench at 51% (Fig. 5**D'**) is slightly grey and EGA-MS shows unexpected amounts of fragments of m/z = 27, 28, 29. Thus, in **D'**, **α**** competes with α, but the residual carbon is oxidized to CO (also detected by EGA-FTIR) and CO_2, in correspondence of a gradual decrease of the TG curve between 400 and 500 °C (Fig. 4**D'**) and, in agreement with literature, only 3-pentanone and CO_2 are detected by EGA-FTIR, thus **α** dominates over **α****.

3.6. Films vs powder

It is important to stress that, due to gas diffusion, films decompose differently than powders, in a given atmosphere. In fact, the decomposition process of $Y(CH_3CH_2CO_2)_3$ for films starts earlier (150 °C versus 250 °C for powders, Fig. 6) but stretches over a wider range of temperatures. As illustrated in Fig. 6a, decomposition shifts to higher temperature as the film thickness increases. The effect seems to be bigger for the step at low temperature, indicating that the thinner the

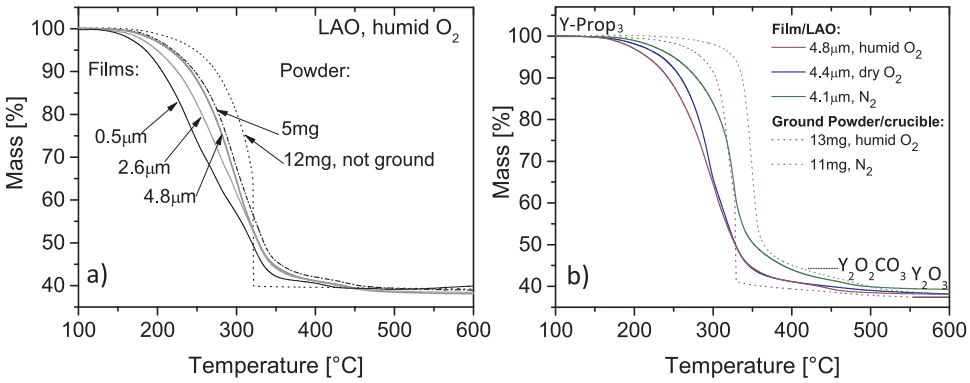

Fig. 6. a) Effect of particles' size and film thickness and b) effect of atmosphere on TG curves of Y-Prop$_3$ at 5 K/min; the legend is labeled in order of curve appearance, from left to right.

film, the earlier the evolution of propionic acid (shifted by 20 °C to lower temperatures when nominal thickness is reduced from 4.8 μm to 0.5 μm). Similarly, for powders deposited on LAO, the decomposition temperature decreases when the particles size is reduced from ≈500 μm to a few μm (by grounding).

Since the kinetics of the **β** reaction scheme is limited by oxygen and water diffusion, the large surface to volume ratio of films makes gas renewal next to the surface much more efficient, favoring this mechanism. For this reason, in films with humid or oxidative atmosphere, only propionic acid is detected, and not 3-pentanone. Route **α** is not seen until the thickness approaches a few microns (≈5 μm) for experiments at atmospheric pressure in N_2, and for very thin films only in experiments performed in vacuum. On the other hand, keeping the mass constant (nominal thickness ≈4.4 μm), the decomposition seems to be accelerated in this order: humid O_2 > dry O_2 > nitrogen/vacuum (Fig. 6b). This is in agreement with the fact that the formation of the radicals, path **α**, requires higher temperatures as compared with hydrolysis and oxidation of the molecule.

In powders, due to the slow intra-particle oxygen transport [21], the local atmosphere near particles is almost inert and process **β** shifts to higher temperatures. This shift of process **β** favors the occurrence of **α**, to the point that in N_2 β is almost suppressed; we observe a long plateau before decomposition starts and the volatiles observed correspond to route **α** (Fig. 4**D'**). As a confirmation, we enhance the inter-particle oxygen transport by spreading particles on a substrate instead of placing them inside a crucible, and we observe in oxygen the same behavior as in films: formation of propionic acid instead of 3-pentanone (Fig. 7**B'**).

The formation of a local inert atmosphere would explain why Nasui et al. [17] reported the presence of ketones by MS instead of propionic acid when the powder sample was decomposed in air. In fact, for powders inside a crucible we observe slight differences between the volatiles formed in oxidizing and inert atmosphere but in all cases ketones and CO_2 are the main volatiles (Fig. 7**C'**, **D'**). However, while in inert conditions most radicals rearrange as 3-pentanone, the presence of oxygen (**C'**, and **C** in smaller amount due to the sensitivity of the film to residual O_2) may oxidize some, resulting in the formation of 2-butanone (reaction scheme **α***) along with the symmetric ketone. In fact, 1) EGA-MS shows the presence of the characteristic fragments of 2-butanone (m/z = 43, 72) well separated from those of 3-pentanone (m/z = 57, 86); 2) additionally the ratio of fragments 43/57 increases by one order of magnitude going from inert to oxidizing atmosphere (from **F**,**E**,**D'** to **C'**), while the 57/86 ratio remains constant; 3) lastly, EGA-FTIR, besides being in agreement with the presence of 2-butanone (Fig. 8**C'**), shows formation of CO and H_2O in **C'** (as expected in **α***), and their contribution decreases with decreasing O_2 content in the atmosphere (going from **C'** to **D'** in Fig. 7). Finally, small amounts of propionic acid and acetaldehyde are also detected by MS and IR at the beginning of

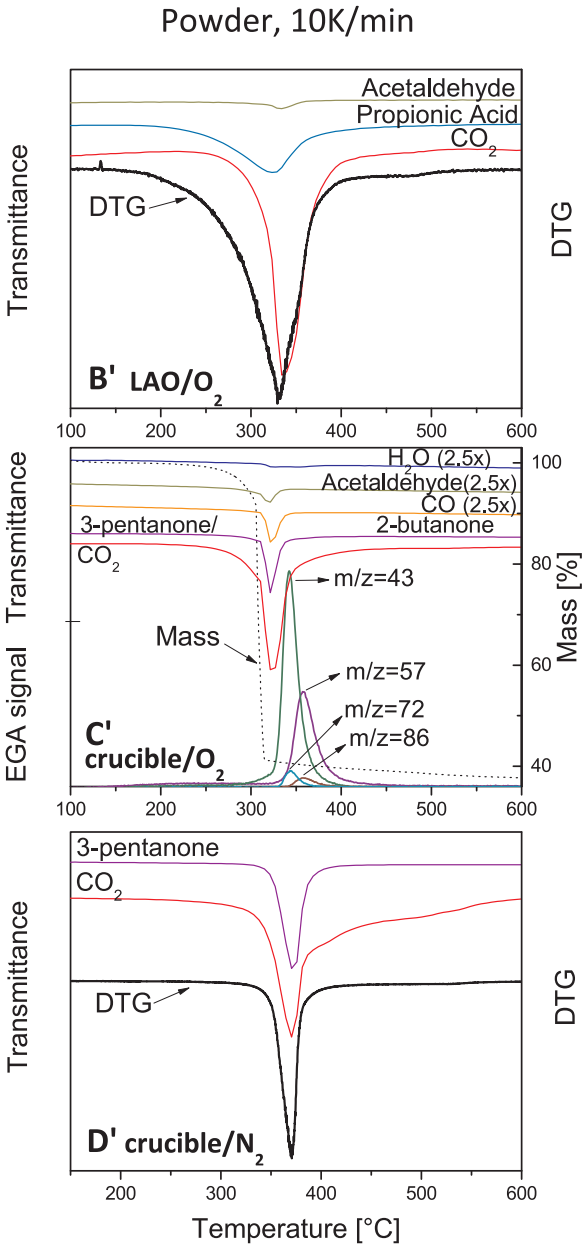

Fig. 7. EGA of the volatiles from decomposition of Y-Prop$_3$ powder at 10 K/min varying atmosphere type and sample layout. Enlarged image of C' can be found in the Supporting Info.

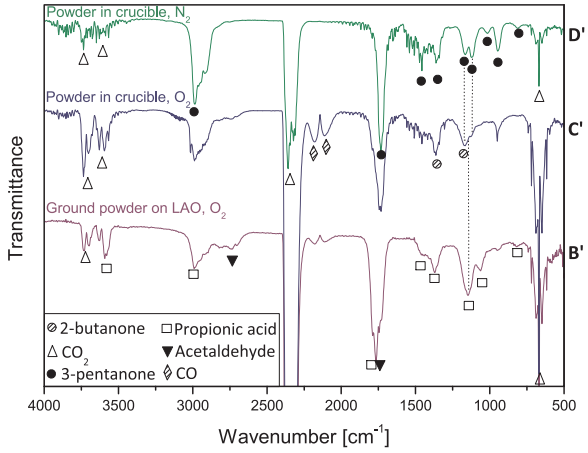

Fig. 8. Infrared spectra of the volatiles detected at the corresponding decomposition peak in Fig. 7.

decomposition in oxygen, as a consequence of the occurrence of reaction scheme **β** at the particles' surface.

Therefore, the significant increase of fragment $m/z = 43$ in the presence of an oxygen atmosphere can be attributed to the oxidation of the C_2H_5 fragment of the ligand to produce acetaldehyde (**A** and **B**), and to yield 2-butanone upon recombination of $CH_3C{=}O\cdot$ and $C_2H_5\cdot$ according to **α*** (in **C**' where radicals are formed). On the other hand, in the absence of oxygen, upon simple recombination without oxidation of the radicals, butane could be formed (in **E**, **F**).

3.7. Thermal explosion

From Fig. 6a, it is apparent that when the powder mass in a humid oxygen atmosphere reaches a critical value, the TG curve no longer exhibits a smooth evolution but shows a very abrupt mass loss and the differential thermal analysis (Supporting Info, Fig.S5) curve exhibits a very sharp exothermic peak; these two features (not observed in N_2) are characteristic of a thermal runaway [21,45–47]. When a thermal runaway occurs, the reaction becomes locally unstable; it reaches a high temperature state and accelerates enormously so that it is virtually adiabatic (all the heat released by the reaction contributes to the sample temperature increase) [48–52].

From the physical parameters of $Y(C_2H_5CO_2)_3$ (Table 2) we calculated the critical film thickness (H_{cr}) at which a thermal runaway would happen for the sample in the form of film in humid O_2, according to the equation [53]:

$$H_{cr} = \frac{R_G T_{Kis}^2}{E_A}\sqrt{\delta_{cr}\frac{ca}{qb}} \quad (1)$$

Furthermore, we were able to calculate the critical mass (m_{cr}) for which thermal explosion would occur in the case of powders in humid O_2 inside a 70-μl alumina pan (finite cylinder geometry, diameter of 4.95 mm) combining the following relationships [53]:

$$m_{cr} = 5\pi\rho a\,\frac{t_R}{\theta_T}\frac{0.878R^2 + 2H^2}{H(1+2\varepsilon)\left\{1-(2+\varepsilon+30\varepsilon^2)\frac{2}{\theta_T}\right\}} \quad \text{and} \quad m_{cr} = \pi\rho R^2 H \quad (2)$$

Table 2
Physical Parameters of $Y(C_2H_5CO_2)_3$.

Specific heat capacity, c [J/(kg K]	1247 (180 °C)
Activation Energy, E_A [kJ/mol]	83.46
Pre-exponential Constant, A [s^{-1}]	4.6×10^5
Enthalpy of Reaction, q [J/kg]	4.26×10^6
Apparent Density, ρ [kg/m^3l]	630
Thermal Conductivity, λ [W/(m·K)]	0.06

where T_{Kis} is the temperature at which the reaction rate is at its maximum [54–56], R_G is the universal gas constant, E_A is the activation energy, a is the thermal diffusivity $\left(a \equiv \frac{\lambda}{\rho c}\right)$, c is the specific heat capacity of the sample, q is the heat of reaction (Enthalpy) and b is the heating rate.

The aforementioned equations and the determination of the physical parameters given in Table 2 are described in the supporting information; in particular, the kinetic parameters (A and E_A) were derived performing TG experiments in humid O_2 at 4 different heating rates, and the curves were analyzed using isoconversional kinetic methods [57,58], specifically the Friedman method. Thermal conductivity (λ) and specific heat capacity (c) were obtained experimentally from differential scanning calorimetry in a specific temperature range for the sample in the form of powder [59,60].

Knowing the aforementioned parameters and solving equation 1, the critical thickness above which combustion would occur for a Y-$Prop_3$ thin film is 937 μm at a heating rate of 5 K/min, which means that for films a thermal explosion is impossible to reach [53,61]. This can be explained thanks to the greater surface of the substrate, which helps dissipating the heat, preventing combustion from occurring. On the other hand, from equation 2, the sample critical mass for Y-$Prop_3$ was found to be around 13 mg for a heating rate of 5 K/min. This is in agreement with the evolution of the TG curve with the sample mass shown in Fig.S2 of the Supporting info, where, for a 13-mg sample, we observe the characteristic sharp mass loss related to a thermal runaway.

4. Conclusions

In this study, we have analyzed the thermal decomposition of yttrium propionate as a function of film thickness, particle size, heating rate and gas atmosphere, comparing samples in the form of film and powder. We have shown that the volatiles depend on the aforementioned parameters. This behavior is related to the competition between two different mechanisms: one related to the hydrolysis and oxidation of yttrium propionate in the presence of water or oxygen, and a second mechanism related to a radical reaction. The first one is enhanced by oxygen and water vapor, and in films due to the easy diffusion of the reacting species. Conversely, the radical decomposition is favored in inert conditions and when oxygen diffusion or atmosphere renewal around the sample are hindered.

Finally, we have observed that films decompose differently than powders; they exhibit different kinetics and the decomposition route is also different. For instance, films decompose at significantly lower temperatures and their decomposition is accelerated by the presence of water vapor. Conversely, within the standard parameters of TG analysis, powders may undergo combustion for sample masses of the order of 10 mg. Taking into account this different behavior between films and powders, it is of the utmost importance to analyze films to disclose the actual phenomena occurring during YBCO precursor pyrolysis in the synthesis of superconducting tapes.

Acknowledgments

This work was funded by the Spanish Programa Nacional de Materiales through the COACHSUPENERGY project (grant numbers MAT2014-51778-C2-1-R and MAT2014-51778-C2-2-R, co-financed by the European Regional Development Fund). It was also supported by the Center of Excellence Severo Ochoa (SEV-2015-0496), the Generalitat of Catalunya (SGR753 and SGR948) and European Union through the projects Eurotapes (EU-FP7 NMP-LA-2012-280432) and Ultrasupertape (ERC ADG-2014-669504).

Appendix A. Supplementary data

Supplementary data associated with this article can be found, in the

online version, at https://doi.org/10.1016/j.jaap.2018.03.021.

References

[1] X. Obradors, T. Puig, Coated conductors for power applications: materials challenges, Sci. Supercond. Technol. 27 (2014) 44003–44019, http://dx.doi.org/10.1088/0953-2048/27/4/044003.

[2] X. Palmer, C. Pop, H. Eloussi, B. Villarejo, P. Roura, J. Farjas, A. Calleja, A. Palau, T. Puig, S. Ricart, Solution design for low-fluorine trifluoroacetate route to YBa2Cu3O7 films, Supercond. Sci. Technol. 29 (2016) 24002, http://dx.doi.org/10.1088/0953-2048/29/2/024002.

[3] L. Ciontea, A. Angrisani, G. Celentano, T. Petrisor jr, A. Rufoloni, A. Vannozzi, A. Augieri, V. Galuzzi, A. Mancini, T. Petrisor, Metal propionate synthesis of epitaxial YBa2Cu3O7-x films, J. Phys. Conf. Ser. 97 (2008) 12302, http://dx.doi.org/10.1088/1742-6596/97/1/012302.

[4] X. Obradors, T. Puig, M. Gibert, A. Queraltó, J. Zabaleta, N. Mestres, Chemical solution route to self-assembled epitaxial oxide nanostructures, Chem. Soc. Rev. 43 (2014) 2200–2225, http://dx.doi.org/10.1039/c3cs60365b.

[5] T. Puig, J.C. Gonzáles, A. Pomar, N. Mestres, O. Castaño, M. Coll, J. Gásquez, F. Sandiumenge, S. Piñol, X. Obradors, The influence of growth conditions on the microstructure and critical currents of TFA-MOD YBa2Cu3O7 films, Supercond. Sci. Technol. 18 (2005) 1141–1150, http://dx.doi.org/10.1088/0953-2048/18/8/020.

[6] T. Araki, I. Hirabayashi, Review of a chemical approach to YBa2Cu3O7-x –coated superconductors — metalorganic deposition using trifluoroacetates, Supercond. Sci. Technol. 16 (2003) 71–94, http://dx.doi.org/10.1088/0953-2048/16/11/r01.

[7] X. Obradors, T. Puig, S. Ricart, M. Coll, J. Gazquez, A. Palau, X. Granados, Growth, nanostructure and vortex pinning in superconducting YBa2Cu3O7 thin films based on trifluoroacetate solutions, Supercond. Sci. Technol. 25 (2012) 123001, http://dx.doi.org/10.1088/0953-2048/25/12/123001.

[8] M. Yoshizumi, I. Seleznev, M.J. Cima, Reactions of oxyfluoride precursors for the preparation of barium yttrium cuprate films, Phys. C 403 (2004) 191–199, http://dx.doi.org/10.1016/j.physc.2003.12.004.

[9] H. Eloussifi, J. Farjas, P. Roura, S. Ricart, T. Puig, X. Obradors, M. Dammak, Thermal decomposition of barium trifluoroacetate thin films, Thermochim. Acta 556 (2013) 58–62, http://dx.doi.org/10.1016/j.tca.2013.01.022.

[10] P. Vermeir, J. Feys, J. Schaubroeck, K. Verbeken, P. Lommens, I. Van Driessche, Influence of sintering conditions in the preparation of acetate-based fluorine-free CSD YBCO films using a direct sintering method, Mater. Res. Bull. 47 (2012) 4376–4382, http://dx.doi.org/10.1016/j.materresbull.2012.09.033.

[11] P. Chu, R.C. Buchanan, Reactive liquid phase sintering of YBa2Cu3O7-x superconducting thin films: part II. Sintering mechanism and film properties, J. Mater. Res. 9 (1994) 844–851, http://dx.doi.org/10.1557/jmr.1994.0844.

[12] P.-Y. Chu, R.C. Buchanan, Reactive liquid phase sintering of solution-derived superconducting thin films: part I. Ambient and precursor effects on BaO-CuO liquid phase formation, J. Mater. Res. 8 (1993) 2134–2142, http://dx.doi.org/10.1557/jmr.1993.2134.

[13] R.B. Mos, M. Nasui, T. Petrisor Jr, M.S. Gabor, R. Varga, L. Ciontea, T. Petrisor, Synthesis, crystal structure and thermal decomposition study of a new barium acetato-propionate complex, J. Anal. Appl. Pyrolysis 92 (2011) 445–449, http://dx.doi.org/10.1016/j.jaap.2011.08.007.

[14] Z. Lin, D. Han, S. Li, Study on thermal decomposition of copper(II) acetate monohydrate in air, J. Therm. Anal. Calorim. 107 (2012) 471–475, http://dx.doi.org/10.1007/s10973-011-1454-4.

[15] M. Nasui, R.B. Mos, T. Petrisor Jr, M.S. Gabor, R.A. Varga, L. Ciontea, T. Petrisor, Synthesis, crystal structure and thermal decomposition of a new copper propionate [Cu(CH3CH2COO)2]·2H2O, J. Anal. Appl. Pyrolysis 92 (2011) 439–444, http://dx.doi.org/10.1016/j.jaap.2011.08.005.

[16] I.A. Martynova, D.M. Tsymbarenko, N.P. Kuz'mina, Yttrium tris propionate monohydrate: synthesis, crystal structure, and thermal stability, Russ. J. Coord. Chem. 40 (2014) 565–570, http://dx.doi.org/10.1134/S1070328414080077.

[17] M. Nasui, C. Bogatan (Pop), L. Ciontea, T. Petrisor, Synthesis, crystal structure modeling and thermal decomposition of yttrium propionate [Y2(CH3CH2COO)6·H2O]·3. 5H2O, J. Anal. Appl. Pyrolysis 97 (2012) 88–93, http://dx.doi.org/10.1016/j.jaap.2012.05.003.

[18] M. Nasui, T. Petrisor Jr, R.B. Mos, A. Mesaros, R.A. Varga, B.S. Vasile, T. Ristoiu, L. Ciontea, T. Petrisor, Synthesis, crystal structure and thermal decomposition kinetics of yttrium propionate, J. Anal. Appl. Pyrolysis 106 (2014) 92–98, http://dx.doi.org/10.1016/j.jaap.2014.01.004.

[19] J. Grivel, Thermal decomposition of yttrium(III) propionate and butyrate, J. Anal. Appl. Pyrolysis 101 (2013) 185–192, http://dx.doi.org/10.1016/j.jaap.2013.01.011.

[20] D.E. Wesolowski, Y.R. Patta, M.J. Cima, Conversion behavior comparison of TFA-MOD and non-fluorine solution-deposited YBCO films, Phys. C Supercond. Its Appl. 469 (2009) 766–773, http://dx.doi.org/10.1016/j.physc.2009.04.008.

[21] P. Roura, J. Farjas, H. Eloussi, L. Carreras, S. Ricart, T. Puig, X. Obradors, Thermal analysis of metal organic precursors for functional oxide preparation: thin films versus powders, Thermochim. Acta 601 (2015) 1–8, http://dx.doi.org/10.1016/j.tca.2014.12.016.

[22] H. Eloussi, J. Farjas, P. Roura, S. Ricart, T. Puig, X. Obradors, M. Dammak, Thermoanalytical study of the decomposition of yttrium trifluoroacetate thin films, Thin Solid Films 545 (2013) 200–204, http://dx.doi.org/10.1016/j.tsf.2013.07.082.

[23] P. Roura, J. Farjas, S. Ricart, M. Aklalouch, R. Guzman, J. Arbiol, T. Puig, A. Calleja, O. Peña-Rodríguez, M. Garriga, X. Obradors, Synthesis of nanocrystalline ceria thin films by low-temperature thermal decomposition of Ce-propionate, Thin Solid Films 520 (2012) 1949–1953, http://dx.doi.org/10.1016/j.tsf.2011.09.058.

[24] D. Sanchez-rodriguez, J. Farjas, P. Roura, S. Ricart, N. Mestres, X. Obradors, T. Puig, Thermal analysis for low temperature synthesis of oxide thin films from chemical solutions, J. Phys. Chem. C 117 (2013) 20133–20138, http://dx.doi.org/10.1021/jp4049742.

[25] J. Farjas, D. Sanchez-Rodriguez, H. Eloussifi, R.C. Hidalgo, P. Roura, S. Ricart, T. Puig, X. Obradors, Can we trust on the thermal analysis of metal organic powders for thin film preparation? in: M. Jain, X. Obradors, Q. Jia, R.W. Schwartz (Eds.), Solut. Synth. Inorg. Film. Nanostructured Mater., MRS Procee, MRS Warrendale, 2012, 2018, pp. 13–18, , http://dx.doi.org/10.1557/opl.2012.919.

[26] H. Fric, M. Jupa, U. Schubert, The solid-state structures of a non-hydrated yttrium carboxylate and an yttrium carboxylate hemihydrate obtained by reaction of yttrium alkoxides with carboxylic acids, Monatshefte Für Chemie – Chem Mon. 137 (2006) 1–6, http://dx.doi.org/10.1007/s00706-005-0400-1.

[27] V. Zeleňák, Z. Vargová, K. Györyová, Correlation of infrared spectra of zinc(II) carboxylates with their structures, Spectrochim. Acta Part A Mol. Biomol. Spectrosc. 66 (2007) 262–272, http://dx.doi.org/10.1016/j.saa.2006.02.050.

[28] E. Gobert-Ranchoux, F. Charbonnier, Comportement thermique des propionates hydrates de calcium, strontium et baryum, J. Therm. Anal. 12 (1977) 33–42, http://dx.doi.org/10.1007/BF01909853.

[29] M. Nasui, C. Bogatan (Pop), L. Ciontea, T. Petrisor, Synthesis, crystal structure modeling and thermal decomposition of yttrium propionate [Y2(CH3CH2COO)6·H2O]·3. 5H2O, J. Anal. Appl. Pyrolysis 97 (2012) 88–93, http://dx.doi.org/10.1016/j.jaap.2012.05.003.

[30] G. Deacon, Relationships between the carbon-oxygen stretching frequencies of carboxylato complexes and the type of carboxylate coordination, Coord. Chem. Rev. 33 (1980) 227–250, http://dx.doi.org/10.1016/S0010-8545(00)80455-5.

[31] K. Nakamoto, Y. Morimoto, A.E. Martell, Infrared spectra of metal chelate compounds. IV. infrared spectra of addition compounds of metallic acetylacetonates 1a, J. Am. Chem. Soc. 83 (1961) 4533–4536, http://dx.doi.org/10.1021/ja01483a010.

[32] I.A. Martynova, D.M. Tsymbarenko, N.P. Kuz'mina, Yttrium tris-propionate monohydrate: synthesis, crystal structure, and thermal stability, Russ. J. Coord. Chem. 40 (2014) 565–570, http://dx.doi.org/10.1134/S1070328414080077.

[33] M. Kakihana, T. Nagumo, Assignment for the infrared spectrum of solid sodium propionate from low-temperature measurements in combination with 13C isotopic shifts, Zeitschrift Für Naturforsch. A 42 (1987) 477–484, http://dx.doi.org/10.1515/zna-1987-0509.

[34] J. Grivel, Thermal decomposition of lutetium propionate, J. Anal. Appl. Pyrolysis 89 (2010) 250–254, http://dx.doi.org/10.1016/j.jaap.2010.08.011.

[35] J. Grivel, Thermal decomposition of Ln(C2H5CO2)3·H2O (Ln = Ho,Er,Tm and Yb), J. Therm. Anal. Calorim. 109 (2012) 81–88, http://dx.doi.org/10.1007/s10973-011-1745-9.

[36] R.A. Hites, K. Biemann, On the mechanism of ketonic decarboxylation. Pyrolysis of Calcium Decanoate, J. Am. Chem. Soc. 94 (1972) 5772–5777, http://dx.doi.org/10.1021/ja00771a039.

[37] M.S. Akanni, E.K. Okoh, H.D. Burrows, H.A. Ellis, The thermal behaviour of divalent and higher valent metal soaps: a review, Thermochim. Acta 208 (1992) 1–41, http://dx.doi.org/10.1016/0040-6031(92)80150-u.

[38] P.A. Barnes, G. Stephenson, S.B. Warrington, The use of TA-GLC-MS as a quantitative specific EGA technique for the investigation of complex thermal decomposition reactions: the thermal decomposition of Calcium propanoate, J. Therm. Anal. 25 (1982) 299–311, http://dx.doi.org/10.1007/bf01912955.

[39] P. Roura, J. Farjas, J. Camps, S. Ricart, J. Arbiol, T. Puig, X. Obradors, Decomposition processes and structural transformations of cerium propionate into nanocrystalline ceria at different oxygen partial pressures, J. Nanopart. Res. 13 (2011) 4085–4096, http://dx.doi.org/10.1007/s11051-011-0352-9.

[40] J.A. Goldsmith, S.D. Ross, Factors affecting the infra-red spectra of some planar anions with D3 h symmetry-III. The spectra of rare-earth carbonates and their thermal decomposition products, Spectrochim. Acta Part A Mol. Spectrosc 23 (1967) 1909–1915, http://dx.doi.org/10.1016/0584-8539(67)80073-4.

[41] G.A.M. Hussein, Formation of high surface-area yttrium oxide by the thermal decomposition of different inorganic precursors, Thermochim. Acta 244 (1994) 139–151, http://dx.doi.org/10.1016/0040-6031(94)80214-9.

[42] N. Imanaka, M. Toshiyuki, Y. Mayama, K. Koyabu, Synthesis of crystalline yttrium oxycarbonate in a single phase, J. Solid State Chem. 178 (2005) 3601–3603, http://dx.doi.org/10.1016/j.jssc.2005.09.024.

[43] S. Liu, R. Jiang, F. Luo, Synthesis and structure of hydrated yttrium carbonate, Y2(CO3)3·2.79H2O, Synth. React. Inorg. Met. Chem. 30 (2000) 271–279, http://dx.doi.org/10.1080/00945710009351762.

[44] Y. Tsukuda, Properties of black Y2O3 sintered bodies, Mater. Res. Bull. 16 (1981) 453–459.

[45] J.P.A. Neeft, F. Hoornaert, M. Makkee, J.A. Moulijn, The effects of heat and mass transfer in thermogravimetrical analysis. A case study towards the catalytic oxidation of soot, Termochimica Acta 287 (1996) 261–278, http://dx.doi.org/10.1016/s0040-6031(96)03002-x.

[46] D. Sánchez-Rodríguez, H. Wada, S. Yamaguchi, J. Farjas, H. Yahiro, Self-propagating high-temperature synthesis of LaMO3 perovskite-type oxide using heteronuclearcyano metal complex precursors, J. Alloy. Compd. 649 (2015) 1291–1299, http://dx.doi.org/10.1016/j.jallcom.2015.07.246.

[47] T. Boddington, F. Hongtu, P.G. Laye, M. Nawaz, D.C. Nelson, Thermal runaway by thermal analysis, Termochim. Acta 170 (1990) 81–87, http://dx.doi.org/10.1016/0040-6031(90)80526-5.

[48] K.C. Patil, S.T. Aruna, T. Mimani, Combustion synthesis: an update, Curr. Opin. Solid State Mater. Sci. 6 (2002) 507–512, http://dx.doi.org/10.1016/S1359-0286(02)00123-7.

[49] O.S. Rabinovich, P.S. Grinchuk, M.A. Andreev, B.B. Khina, Conditions for

combustion synthesis in nanosized Ni/Al films on a substrate, Phys. B 392 (2007) 272–280, http://dx.doi.org/10.1016/j.physb.2006.11.032.
[50] L. Thiers, A.S. Mukasyan, A. Varma, Thermal explosion in Ni-Al system: influence of reaction medium microstructure, Combust. Flame 131 (2002) 198–209, http://dx.doi.org/10.1016/s0010-2180(02)00402-9.
[51] N. Semenov, Thermal theory of combustion and explosion, Prog. Phys. Sci. 23 (1940).
[52] N. Semenov, Theories of combustion processes, Zeitschrift Für Phys. 48 (1928) 571–582.
[53] D. Sánchez-Rodriguez, J. Farjas, P. Roura, The critical conditions for thermal explosion in a system heated at a constant rate, Combust. Flame 18 (2017) 211–219, http://dx.doi.org/10.1016/j.combustflame.2017.08.008.
[54] H.E. Kissinger, Reaction kinetics in differential thermal analysis, Anal. Chem. 29 (1957) 1702–1706, http://dx.doi.org/10.1021/ac60131a045.
[55] P. Roura, J. Farjas, Analytical solution for the Kissinger equation, J. Mater. Res. 24 (2009) 3095–3098, http://dx.doi.org/10.1557/JMR.2009.0366.
[56] J. Farjas, P. Roura, Exact analytical solution for the Kissinger equation: determination of the peak temperature and general properties of thermally activated transformations, Thermochim. Acta 598 (2014) 51–58, http://dx.doi.org/10.1016/j.tca.2014.10.024.
[57] J. Farjas, P. Roura, Isoconversional analysis of solid state transformations. A critical review Part II. Complex transformations, J. Therm. Anal. Calorim. 105 (2011) 767–773, http://dx.doi.org/10.1007/s10973-011-1447-3.
[58] J. Farjas, P. Roura, Isoconversional analysis of solid state transformations. A critical review Part I. Single step transformations with constant activation energy, J. Therm. Anal. Calorim. 105 (2011) 757–766, http://dx.doi.org/10.1007/s10973-011-1446-4.
[59] M. Pujula, D. Sánchez-Rodríguez, J.P. Lopez-Olmedo, J. Farjas, P. Roura, Measuring thermal conductivity of powders with differential scanning calorimetry, J. Therm. Anal. Calorim. 125 (2016) 571–577, http://dx.doi.org/10.1007/s10973-016-5274-4.
[60] D. Sánchez-Rodríguez, J.P. López-Olmedo, J. Farjas, P. Roura, Determination of thermal conductivity of powders in different atmospheres by differential scanning calorimetry, J. Therm. Anal. Calorim. 121 (2015) 469–473, http://dx.doi.org/10.1007/s10973-015-4429-z.
[61] D. Sánchez-Rodriguez, J. Farjas, P. Roura, The critical condition for thermal explosion in an isoperibolic system, AlChE J. 63 (2017) 3979–3993, http://dx.doi.org/10.1002/aic.15727.